nature portfolio

https://doi.org/10.1038/s41567-022-01544-9

Supplementary information

Simulation of open quantum systems by automated compression of arbitrary environments

In the format provided by the authors and unedited

Supplementary material: Simulation of open quantum systems by automated compression of arbitrary environments

S.1. CALCULATION OF INTERMEDIATE-TIME CLOSURES

In Eq. (18) we gave an expression for the reduced system density matrix at time t_n using the process tensor (PT) for n time steps. In practical applications, it is desirable to also be able to calculate the reduced system density matrix at intermediate times t_l to extract the full dynamics of the system. Here we show how this can be extracted. As a reminder, in the following we use the symbols ν or μ to enumerate system states, and ξ or η for environment states.

The calculation of ρ_{α_l} for $l < n$ requires the knowledge of a PT for l time steps. From Eq. (19) it is clear that, before any matrix product operator (MPO) compression, the PT for l time steps can be obtained from the PT for $n > l$ time steps by tracing over the environment at that step, $\sum_{\xi_l,\eta_l} \delta_{\xi_l,\eta_l}$. After compression, it is less clear how this trace is to be executed on the inner indices d_l. In principle, it is possible to track how the trace operation transforms under the individual MPO compression steps. A more practical alternative is to make use of the unitarity of the environment evolution and recursively obtain the PT for $n-1$ time steps from the PT for n time steps.

Consider the terms corresponding to the last time step in Eq. (19):

$$\sum_{\xi_n\eta_n} \delta_{\xi_n\eta_n} A^{\nu_n\tilde{\nu}_n}_{\xi_n\xi_{n-1}} A^{\mu_n\tilde{\mu}_n *}_{\eta_n\eta_{n-1}} = \sum_{\xi} \langle\tilde{\mu}_n, \eta_{n-1}| e^{\frac{i}{\hbar}H_E\Delta t} |\mu_n, \xi\rangle\langle\nu_n, \xi| e^{-\frac{i}{\hbar}H_E\Delta t} |\tilde{\nu}_n, \xi_{n-1}\rangle. \tag{S.1.1}$$

Performing the trace over the system states $\sum_{\nu_n,\mu_n} \delta_{\nu_n\mu_n}$ in addition to the trace over the environment states yields

$$\begin{aligned}\sum_{\nu_n\mu_n} \delta_{\nu_n\mu_n} \sum_{\xi_n\eta_n} \delta_{\xi_n\eta_n} A^{\nu_n\tilde{\nu}_n}_{\xi_n\xi_{n-1}} A^{\mu_n\tilde{\mu}_n *}_{\eta_n\eta_{n-1}} =& \langle\tilde{\mu}_n, \eta_{n-1}| e^{\frac{i}{\hbar}H_E\Delta t} \left[\sum_{\nu,\xi} |\nu,\xi\rangle\langle\nu,\xi|\right] e^{-\frac{i}{\hbar}H_E\Delta t} |\tilde{\nu}_n, \xi_{n-1}\rangle \\ =& \langle\tilde{\mu}_n, \eta_{n-1}| e^{\frac{i}{\hbar}H_E(\Delta t-\Delta t)} |\tilde{\nu}_n, \xi_{n-1}\rangle = \langle\tilde{\mu}_n, \eta_{n-1}|\tilde{\nu}_n, \xi_{n-1}\rangle = \delta_{\tilde{\mu}_n\tilde{\nu}_n}\delta_{\eta_{n-1}\xi_{n-1}}.\end{aligned} \tag{S.1.2}$$

Together with the sum over the η_{n-1} and ξ_{n-1} in the $(n-1)$-th time step in the PT, the term $\delta_{\eta_{n-1}\xi_{n-1}}$ again becomes equivalent to calculating the trace over the environment modes, but at time step $n-1$. Therefore, the PT for $n-1$ time steps can be related to the PT for n time steps by

$$I^{(\nu_{n-1}\tilde{\nu}_{n-1})\ldots(\nu_1\tilde{\nu}_1)}_{(\mu_{n-1}\tilde{\mu}_{n-1})\ldots(\mu_1\tilde{\mu}_1)} = \sum_{\nu_n\mu_n} \delta_{\nu_n\mu_n} I^{(\nu_n\tilde{\nu})(\nu_{n-1}\tilde{\nu}_{n-1})\ldots(\nu_1\tilde{\nu}_1)}_{(\mu_n\tilde{\nu})(\mu_{n-1}\tilde{\mu}_{n-1})\ldots(\mu_1\tilde{\mu}_1)}, \tag{S.1.3}$$

where $\tilde{\nu}$ is an arbitrary system state, which we choose as $\tilde{\nu} = 0$. As this expression only involves outer indices and is independent of the inner indices, it applies equally to the PT after MPO compression. Thus, given the PT for n time steps in MPO form in Liouville space

$$\mathcal{I}^{(\alpha_n,\tilde{\alpha}_n)(\alpha_{n-1},\tilde{\alpha}_{n-1})\ldots(\alpha_1,\tilde{\alpha}_1)} = \sum_{d_{n-1}\ldots d_1} \mathcal{Q}^{(\alpha_n,\tilde{\alpha}_n)}_{1d_{n-1}} \mathcal{Q}^{(\alpha_{n-1},\tilde{\alpha}_{n-1})}_{d_{n-1}d_{n-2}} \ldots \mathcal{Q}^{(\alpha_1,\tilde{\alpha}_1)}_{d_1 1}, \tag{S.1.4}$$

we can obtain the PT for l time steps as

$$\mathcal{I}^{(\alpha_l,\tilde{\alpha}_l)(\alpha_{l-1},\tilde{\alpha}_{l-1})\ldots(\alpha_1,\tilde{\alpha}_1)} = \sum_{d_l\ldots d_1} q_{d_l} \mathcal{Q}^{(\alpha_l,\tilde{\alpha}_l)}_{d_l d_{l-1}} \mathcal{Q}^{(\alpha_{l-1},\tilde{\alpha}_{l-1})}_{d_{l-1}d_{l-2}} \ldots \mathcal{Q}^{(\alpha_1,\tilde{\alpha}_1)}_{d_1 1}, \tag{S.1.5}$$

where the closures q_{d_l} are calculated recursively via

$$q_{d_n=1} = 1 \tag{S.1.6}$$

$$q_{d_{l-1}} = \sum_{d_l} q_{d_l} \sum_{\alpha_l\nu_l} \delta_{\alpha_l,(\nu_l,\nu_l)} \mathcal{Q}^{(\alpha_l 0)}_{d_l d_{l-1}}. \tag{S.1.7}$$

With the closures q_{d_l} the reduced system density matrix ρ_{α_l} at time step t_l can be extracted from the propagated quantities $\mathcal{R}_{\alpha_l d_l}$ defined in Eq. (19) as

$$\rho_{\alpha_l} = \sum_{d_l} q_{d_l} \mathcal{R}_{\alpha_l d_l}. \tag{S.1.8}$$

S.2. NUMERICAL CONVERGENCE OF THE ACE ALGORITHM

The ACE algorithm, as described in the main text, is numerically convergent in the following sense: Every step in the derivation that involves an approximation is controlled by convergence parameters, such that in principle the error can be made arbitrarily small as the corresponding convergence parameters are taken to zero or infinity as appropriate. Thus, in principle, exact results can be approximated to arbitrary precision given enough computational resources.

In this section we first review the sources of numerical error that exist—time discretisation, MPO compression, and discretisation of a continuum of environment modes. We then present a study of the tradeoff between accuracy and the computational cost of a calculation.

A. Sources of numerical error

1. Time discretization

The starting point of the derivation of ACE is the introduction of an equidistant time grid $t_n = n\Delta t$, defined by a time step width Δt. The maximal number of time steps $n_{\max}$ then determines the simulation end time $t_e = n_{\max}\Delta t$. Decomposing the total time evolution operator into system and environment parts for a time step Δt introduces numerical Trotter errors. For the system–environment decomposition we use a first-order expansion

$$e^{-\frac{i}{\hbar}(H_S+H_E)\Delta t} = e^{-\frac{i}{\hbar}H_E\Delta t}e^{-\frac{i}{\hbar}H_S\Delta t} + \mathcal{E}^{SE}_{\text{Trotter}} \tag{S.2.1}$$

while between different environment modes we use a second-order expansion

$$e^{-\frac{i}{\hbar}\left(H_E[K-1]+H_E^K\right)\Delta t} = e^{-\frac{i}{\hbar}H_E[K-1]\frac{\Delta t}{2}}e^{-\frac{i}{\hbar}H_E^K\Delta t}e^{-\frac{i}{\hbar}H_E[K-1]\frac{\Delta t}{2}} + \mathcal{E}^{K}_{\text{Trotter}}. \tag{S.2.2}$$

While there has been considerable work on finding rigorous bounds for Trotter errors (see e.g. Childs *et al.* [1] and references therein), here we limit our discussion to a simple analysis in terms of a Taylor expansion orders. This yields single-step error terms of the order $\mathcal{E}^{SE}_{\text{Trotter}} = \mathcal{O}(\Delta t^2)$ and $\mathcal{E}^{K}_{\text{Trotter}} = \mathcal{O}(\Delta t^3)$, respectively. Regarding the system–environment decoupling we may note however, that when the full time evolution up to the final time t_e is considered, the product

$$P_1 := \left(e^{-\frac{i}{\hbar}H_E\Delta t}e^{-\frac{i}{\hbar}H_S\Delta t}\right)\left(e^{-\frac{i}{\hbar}H_E\Delta t}e^{-\frac{i}{\hbar}H_S\Delta t}\right)\ldots\left(e^{-\frac{i}{\hbar}H_E\Delta t}e^{-\frac{i}{\hbar}H_S\Delta t}\right) \tag{S.2.3}$$

is related to the product obtained by symmetric Trotter decomposition

$$P_2 :=\left(e^{-\frac{i}{\hbar}H_S\frac{\Delta t}{2}}e^{-\frac{i}{\hbar}H_E\Delta t}e^{-\frac{i}{\hbar}H_S\frac{\Delta t}{2}}\right)\left(e^{-\frac{i}{\hbar}H_S\frac{\Delta t}{2}}e^{-\frac{i}{\hbar}H_E\Delta t}e^{-\frac{i}{\hbar}H_S\frac{\Delta t}{2}}\right)\ldots\left(e^{-\frac{i}{\hbar}H_S\frac{\Delta t}{2}}e^{-\frac{i}{\hbar}H_E\Delta t}e^{-\frac{i}{\hbar}H_S\frac{\Delta t}{2}}\right), \tag{S.2.4}$$

by the relation $P_2 = e^{-\frac{i}{\hbar}H_S\frac{\Delta t}{2}}P_1e^{+\frac{i}{\hbar}H_S\frac{\Delta t}{2}}$. Thus, the results obtained by first-order Trotter decomposition converge identically to those obtained by a second-order Trotter decomposition, up to evolving the initial and final states by a half time step.

By keeping the final time t_e fixed and expressing the time step width $\Delta t = t_e/n_{\max}$, the total error accumulated can be written in terms of the total number of time steps $n_{\max}$. For the second-order Trotter decomposition the total error is $\left|e^{-\frac{i}{\hbar}(H_S+H_E)t} - P_2\right| = n_{\max}\,\mathcal{O}(1/n_{\max}^3) = \mathcal{O}(1/n_{\max}^2)$. As the environment propagator $e^{-\frac{i}{\hbar}H_E\Delta t}$ itself is also approximated up to an error $\mathcal{O}(1/n_{\max}^3)$— arising from decomposing it into different modes— the overall Trotter error accumulated during the simulation scales as $\mathcal{O}(1/n_{\max}^2)$. This error can thus be made arbitrarily small by choosing a fine enough time discretisation.

2. MPO compression

A second source of numerical error occurs when the MPO representing the process tensor is compressed. This compression is done using a singular value decomposition (SVD), and truncation by neglecting singular values below a given threshold. A sequential sweep of SVDs is performed across the MPO.

For a single SVD step the Eckart–Young–Mirsky theorem [2] provides concrete error bounds: Given the SVD of a matrix A, we define

$$A = U\Sigma V^\dagger = \sum_{i=1}^{n} \sigma_i u_i v_i^\dagger = \underbrace{\sum_{i=1}^{k} \sigma_i u_i v_i^\dagger}_{=:\tilde{A}} + \underbrace{\sum_{i=k+1}^{n} \sigma_i u_i v_i^\dagger}_{=:\delta A}, \tag{S.2.5}$$

where σ_i are the singular values in descending order, u_i, v_i the corresponding singular vectors, and k is the smallest number such that $\sigma_i < \epsilon\sigma_1$ for all $i > k$. $\tilde{A}$ represents the relevant part of the matrix A, whereas δA is considered irrelevant and is therefore neglected. The Eckart–Young–Mirsky theorem states that the matrix $\tilde{A}$ provides the best approximation to A of all matrices with rank k. In particular, the error in the spectral norm is $\|A - \tilde{A}\|_2 = \sigma_{k+1}$ while for the Frobenius norm $\|A - \tilde{A}\|_F = \sqrt{\sigma_{k+1}^2 + \sigma_{k+2}^2 + \cdots + \sigma_n^2}$. In any case, for $\epsilon \to 0$ one finds $\|A - \tilde{A}\| \to 0$ and the low-rank approximation $\tilde{A} \to A$ becomes exact.

Exact bounds for the accumulated error of a full line sweep are more difficult to assess. This is because, e.g., in a sweep from right to left, the next matrix is multiplied with vectors $\sigma_i u_i$ $(i = 1, 2, \ldots, k)$ from the SVD of the previous matrix, so the result depends on the overlap between u_i and the row vectors of the next matrix. Furthermore, it is a priori not clear how strongly a given matrix element of the PT MPO contributes to the reduced system density matrix at a given point in time, in particular because this also depends on the concrete system Hamiltonian H_S. It also remains an open question how numerical errors propagate, e.g., if small deviations from Hermitianity and positivity of the density matrices grow exponentially or behave more advantageously.

A rigorous mathematical analysis of the error bounds for tensor network methods is beyond the scope of the present article. Yet, it is clear that the MPO compressed object turns into an exact reformulation of the original uncompressed PT in the limit $\epsilon \to 0$. As such, in this work, we restrict further analysis to numerical convergence tests.

3. Continuum discretisation

While some open quantum systems, such as the example of spin baths in the main text, contain a finite number of environment modes, others involve a continuum of modes that require discretisation in order to apply the ACE algorithm. For this discretisation to converge numerically, one has to additionally demand piecewise continuity of the environment initial state as well as the environment Hamiltonian with respect to the index $\mathbf{k}$ describing the continuum.

B. Numerical convergence and computational cost

To numerically test the convergence of ACE with respect to different convergence parameters, we consider again the example of the resonant level model (first example in the main text). In particular, we focus on the case of band width $\omega_{BW} = 10\gamma$, where visible deviations from the Markovian result can be seen.

First, using $N_E = 10$ modes to discretise the continuum and fixed final time $\gamma t_e = 2.5$, we investigate the numerical error for different time step widths Δt and MPO compression thresholds ϵ. Here, we define the error as

$$\text{Error} = \max_i \left| n_S\big(t_i, \{\Delta t, \epsilon\}\big) - n_S\big(t_i, \{\Delta t, \epsilon_{\min}\}\big) \right|, \tag{S.2.6}$$

where $n_S\big(t_i, \{\Delta t, \epsilon\}\big)$ is the system site occupation at time $t_i = i\Delta t$ calculated using the set of convergence parameters $\{\Delta t, \epsilon\}$. Because the computation time and the convergence with respect to the threshold ϵ differ vastly for different time discretisations Δt, we use reference calculations with different $\epsilon_{\min}$ for each Δt. Specifically we use $\epsilon_{\min}(\gamma\Delta t = 0.1) = 3 \times 10^{-9}$, $\epsilon_{\min}(\gamma\Delta t = 0.05) = 3 \times 10^{-10}$, and $\epsilon_{\min}(\gamma\Delta t = 0.01) = \epsilon_{\min}(\gamma\Delta t = 0.005) = \epsilon_{\min}(\gamma\Delta t = 0.001) = 10^{-11}$.

These numerical errors vs compression threshold ϵ are depicted in Fig. S.2.1**a** on a double logarithmic scale. As expected, the numerical error generally decreases as the threshold is reduced. The threshold needed to obtain a given numerical accuracy is found to depend strongly on the time step width Δt. Furthermore, a common feature in all curves is that there exists a plateau where for a broad range of thresholds no significant gain in accuracy is observed.

These facts can be explained by the distribution of singular values: The uncompressed PT MPO matrices are directly related to the environment propagator, which for very small time steps can be approximated as $e^{-\frac{i}{\hbar}H_E\Delta t} \approx 1 - \frac{i}{\hbar}H_E\Delta t$ and therefore possesses matrix elements (diagonals) of order 1 as well as contributions (off-diagonals) of order $\|H_E\|\Delta t/\hbar$, but hardly any elements in the intermediate range. Matrix elements of vastly different orders of

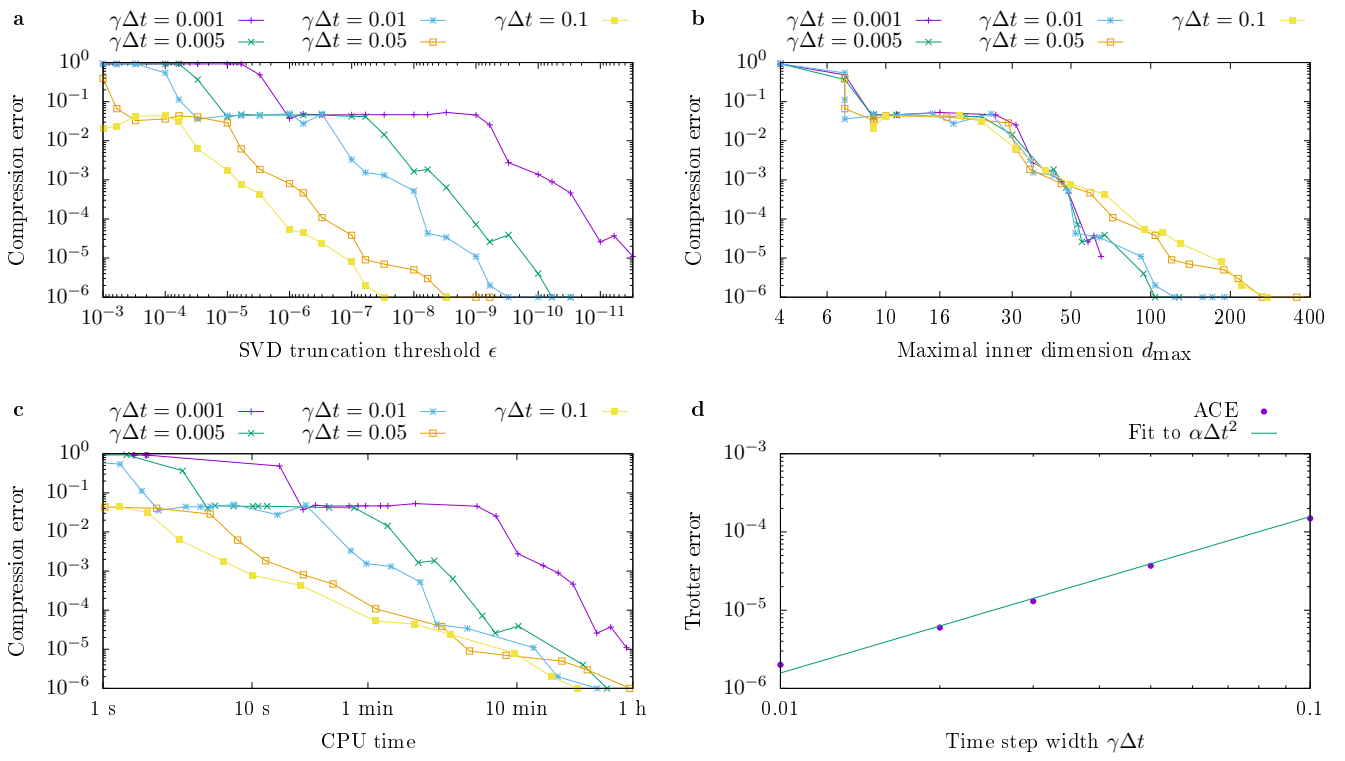

FIG. S.2.1. Convergence of ACE simulations with respect to SVD truncation threshold ϵ (panel **a**). Note the horizontal axis goes from largest ϵ to smallest. The same results are also plotted as a function of the maximal inner dimension $d_{\max}$ (panel **b**) and the total CPU time (panel **c**) needed for the calculations on a conventional laptop computer with Intel Core i5-8265U. The error associated with the time discretisation (Trotter error) is depicted in panel **d**.

magnitude translate into singular values of different orders of magnitude, leading to a corresponding gap in the SVD spectrum. This analysis also demonstrates that smaller time steps require smaller convergence thresholds to produce the same level of accuracy, to avoid terms of the order $\|H_E\|\Delta t/\hbar \lesssim \epsilon$ being disregarded.

Figure S.2.1**b** depicts the results of the same calculations plotted against the maximal inner dimension $d_{\max}$ of the PT. Displayed in this way, the curves calculated for different time step widths Δt all nearly overlap, suggesting that the maximal inner dimension is a more reliable measure of the numerical accuracy than the compression threshold ϵ itself. Note, however, that in our fixed-precision algorithm, $d_{\max}$ is not known a priori.

For practical applications it is important to relate these parameters controlling precision to the computation time needed to perform ACE simulations. We therefore also present the numerical error of the above calculations as a function of the CPU time in Fig. S.2.1**c**. These were obtained on a conventional laptop computer with Intel Core i5-8265U processor. For a given accuracy, the fastest computation is achieved for the largest time steps because the PT MPO has fewer sites and, thus, fewer SVDs to perform. In particular, for this problem, we find that very accurate results are achievable within minutes of computation time.

Figure S.2.1**d**, shows the Trotter error $\max_i \left|n_S\big(t_i, \{\Delta t, \epsilon_{\min}\}\big) - n_S\big(t_i, \{\Delta t_{\min}, \epsilon_{\min}\}\big)\right|$ defined as the difference with respect to reference calculations with time step width $\gamma\Delta t_{\min} = 0.005$, where for given Δt the corresponding best converged results with smallest threshold $\epsilon_{\min}$ is used. The theoretical expectation that the accumulated Trotter error is proportional to Δt^2 (or $1/n_{\max}^2$) is corroborated by a fit of the data points to this trend.

Finally, we numerically investigate the convergence of the PT with respect to the mode discretisation of a continuum of environment modes. Figure S.2.2**a** shows the time evolution of the system occupation for the same Fermionic open quantum system as discussed above. Results are shown up to final time $\gamma t_e = 5$ using a fixed compression threshold $\epsilon = 10^{-6}$ and a fixed time step width $\gamma\Delta t = 0.05$, comparing the results for different numbers of environment modes N_E spanning the total band with $\omega_{BW} = 10\gamma$. For a large number of modes $N_E = 100$ the results shown in the main text are reproduced, i.e. system occupation grows roughly as predicted by the Markovian limit $1 - e^{-\gamma t}$, albeit with visible deviations. However, if the continuum discretisation is too coarse as in the case $N_E = 2$, the description is only accurate for a short time, after which strong deviations occur. For small N_E this is inevitable, because there is a limited set of degrees of freedom, corresponding to a limited set of frequencies controlling the dynamics of the

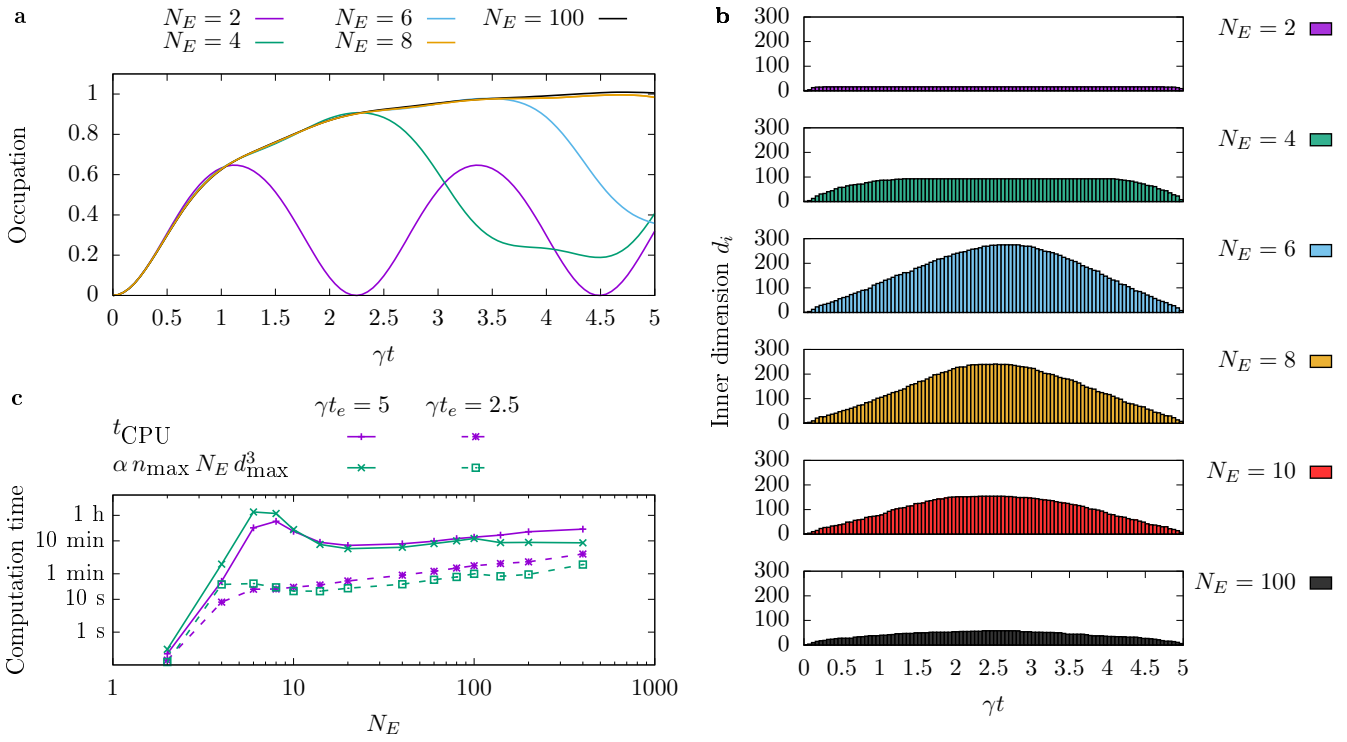

FIG. S.2.2. Convergence of ACE simulations with respect to the number of modes N_E used to discretise a continuum. Panel **(a)** compares the time dependence of occupation for different values of N_E. Panel **(b)** shows how N_E affects the inner dimensions of the MPO, while panel **(c)** shows how this affects the computation time required.

system. With increasing number of modes N_E, the time at which these strong deviations appear becomes later. Here, for $N_E = 8$ this point is almost beyond the final time t_e, so a good description of environment effects is retained for the full simulation.

The mode discretisation has a significant impact on the structure of the process tensor. In Fig. S.2.2**b**, the inner dimension d_i at every time step t_i is depicted. The typical shape of the d_i distribution is roughly trapezoidal; this reflects the constraint in the bond dimension near the ends of the MPO, so that the maximum inner dimension $d_{\max}$ occurs near the centre of the MPO. Notably, we find that increasing the number of modes leads first to an increase in $d_{\max}$ up to a certain N_E after which $d_{\max}$ begins to decrease. The initial increase can be explained by the PT including more and more degrees of freedom. The eventual decrease is due to dephasing between modes with similar frequencies. This result is consistent with recent results by Ye and Chan [3]. The largest values of $d_{\max}$ are found at similar values of N_E to the conditions where convergence of the result with N_E is first reached, as seen in Fig. S.2.2**a**.

The dependence of the inner dimensions of the PT on the mode discretisation has a significant impact on the computational resources required for the ACE method. Figure S.2.2**c** shows the CPU time needed for carrying out the ACE simulation for two different final times $\gamma t_e = 5$ and $\gamma t_e = 2.5$. The computation time is found to increase rapidly with N_E when N_E is small, but then reach an approximate plateau at large N_E. (The required computation time can even have a minimum, as seen around $N_E = 20$ in the case $\gamma t_e = 5$.) These trends can be explained by a simple scaling argument: Exact SVD routines scale as d^3 where d is the matrix dimension. The number of SVDs performed in total is proportional to the number of time steps $n_{\max}$ times the number of environment modes N_E. Using the maximal inner dimension $d_{\max}$ as a proxy for the typical dimension, one expects the computation time to scale as $t_{\mathrm{estimate}} = \alpha\, n_{\max} N_E d_{\max}^3$. With $d_{\max}$ extracted from the simulations, t_{estimate} is fit against the CPU times of the curve for $\gamma t_e = 5$. This is depicted in Fig. S.2.2**c**. We find that this formula, with a constant α, indeed captures the trends in the computation time well.

S.3. RUN TIMES AND COMPARISON TO GAUSSIAN METHODS

A. Run time for examples provided

Example	Run time
Resonant level model:	
$N_E = 2$	< 1 s
$N_E = 4$	4 s
$N_E = 10$	56 s
$N_E = 100$	13 h 3 min
Phonons & photons:	
Construct PT phonons	1 h 14 min
Construct PT photons, $\omega_{BW} = 10$ ps^{-1}	10 h 47 min
Construct PT photons, $\omega_{BW} = 0.4$ ps^{-1}	17 s
Contraction of PT (combined)	40 s
[iQUAPI: phonons]	[1 min 0 s]
Spins, fully polarised:	
$N = 10$, $\epsilon = 10^{-10}$	1 min 10 s
$N = 100$, $\epsilon = 10^{-10}$	4 min 09 s
$N = 1000$, $\epsilon = 10^{-10}$	13 min 50 s
Spins, partially polarised:	
$N = 10$, $\epsilon = 10^{-10}$	3 min 32 s
$N = 10$, $\epsilon = 10^{-13}$	19 min 59 s
$N = 10$, $\epsilon = 10^{-16}$	1 h 45 min
$N = 100$, $\epsilon = 10^{-10}$	5 min 30 s
$N = 100$, $\epsilon = 10^{-13}$	33 min 12 s
$N = 100$, $\epsilon = 10^{-16}$	2 h 28 min
Spins, unpolarised:	
$N = 10$, $\epsilon = 10^{-10}$	5 min 21 s
$N = 10$, $\epsilon = 10^{-13}$	34 min 2 s
$N = 10$, $\epsilon = 10^{-16}$	4 h 40 min
$N = 100$, $\epsilon = 10^{-10}$	8 min 27 s
$N = 100$, $\epsilon = 10^{-13}$	40 min 52 s
$N = 100$, $\epsilon = 10^{-16}$	3 h 8 min

Example	Run time
Morse potential:	
SBM, $M = 5$	20 min 17 s
HO, $M = 5$	23 min 30 s
$\Lambda = 2$, $M = 2$	3 min 39 s
$\Lambda = 2$, $M = 2$, renorm.	3 min 48 s
$\Lambda = 3$, $M = 3$	22 min 39 s
$\Lambda = 3$, $M = 3$, renorm.	21 min 58 s
$\Lambda = 4$, $M = 4$	1 h 37 min
$\Lambda = 4$, $M = 4$, renorm.	1 h 36 min
$\Lambda = 5$, $M = 5$	4 h 4 min
$\Lambda = 5$, $M = 5$, renorm.	3 h 48 min
$\Lambda = 10$, $M = 5$	1 h 6 min
$\Lambda = 10$, $M = 5$, renorm.	1 h 7 min
$\Lambda = 100$, $M = 5$	33 min 15 s
$\Lambda = 100$, $M = 5$, renorm.	32 min 15 s
Superradiance:	
Construct PT	31 min 39 s
Contraction of PT	2 s
Dispersive coupling:	
single mode	7 s
instant. Fock	2 s
pulsed, no losses	23 min 36 s
pulsed, with losses	13 min 2 s

TABLE S.3.1. Run times for the examples discussed in the main text and the Supplementary Material. In some examples ("phonons & photons" and "superradiance"), we use the fact that the construction of the process tensor ("Construct PT") using ACE and the subsequent contraction to determine time evolution can be separated. This separation is useful when one environment is used multiple times with different system Hamiltonians.

The simulations for this article are performed on a conventional laptop computer with Intel i5-8265U processor and 16 GB of RAM. The ACE code is available at Ref. [4]. The numerically most demanding part, the MPO compression using SVDs, is done using the `JacobiSVD` routine provided by the Eigen library (version 3.4-rc1), which calls the corresponding LAPACK routines when compiled and linked appropriately. Here, we use the LAPACK implementation provided by the Intel MKL (version 2021.3.0). The C++ code is compiled and linked using the GCC compiler (version 9.3.0).

The run times of the simulations for the examples discussed in the main text as well as in other sections of the Supplemental Material are listed in Tab. S.3.1. As can be seen, typical calculation times for these examples range between minutes to several hours, demonstrating the efficiency and practicability of ACE over a broad range of different physical systems. The challenging simulations of spin baths with tiny thresholds $\epsilon = 10^{-16}$ require more than the physical 16 GB of RAM, and so the times observed here are affected by swapping to disk. Note that swapping is efficient for ACE simulations because a single MPO compression step only modifies a single MPO matrix at a time.

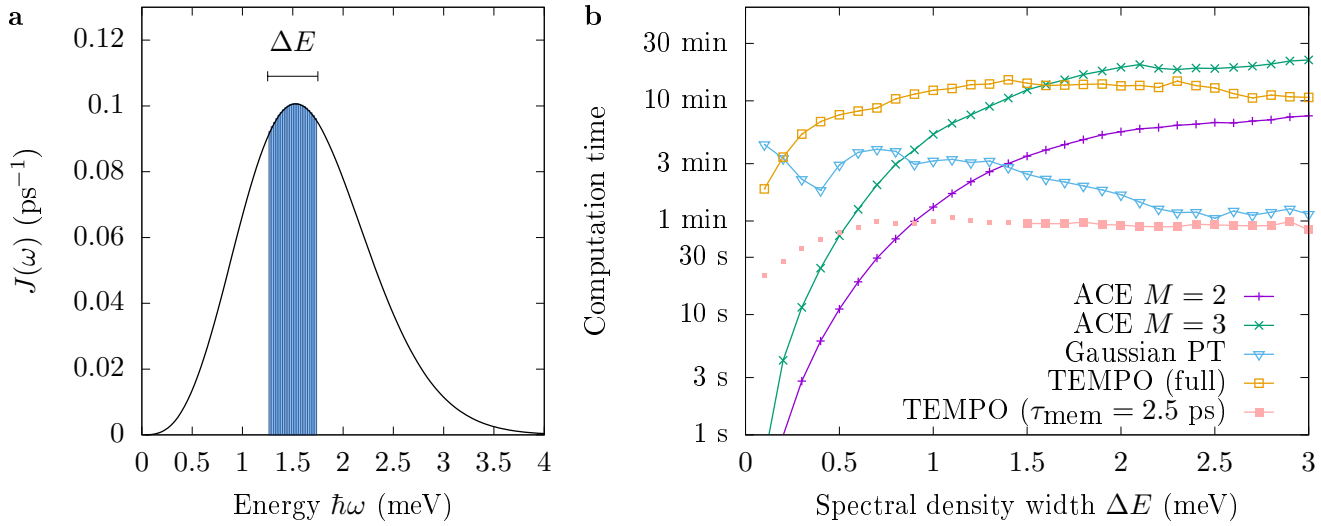

FIG. S.3.1. Comparison of different numerically convergent methods for Gaussian environments: ACE, Gaussian PT calculation, and TEMPO for the example of an off-resonantly driven quantum dot coupled to a bath of phonons. To control the non-Markovianity of the bath, the spectral density is manually restricted to a finite spectral range ΔE centred around the energy $\hbar\delta = 1.5$ meV corresponding to the detuning of the excitation, as depicted in panel **a**. The corresponding computation times are shown in panel **b**.

B. Comparison with numerically convergent methods for Gaussian baths

In the special case of Gaussian environments, other numerically convergent methods have been established such as the calculation of PTs for Gaussian baths devised by Jørgensen and Pollock [5] building on the TEMPO algorithm [6], which itself is a reformulation of the iterative path integral approach iQUAPI [7]. In such methods, the augmented density matrix is presented, compressed, and propagated in MPO representation. An implementation of these two methods is incorporated into our ACE computer code [4].

These methods rely on the fact that for Gaussian baths, the path integral over the environment can be solved analytically, giving explicit expressions for the Feynman-Vernon influence functional. As all these methods are numerically convergent, it is an interesting question which method performs best (requires least computation time) in which situation—restricting to Gaussian cases where all methods are available. To this end, we consider again the example of the quantum dot coupled to phonons and subject to radiative losses discussed in the main text, focusing on the numerically convergent modelling of phonon effects while losses are accounted for by Lindblad terms. Anticipating that the performance of the different methods strongly depends on the memory time of the environment, we perform calculations for various widths of the spectral density. As depicted in Fig. S.3.1**a**, we use the envelope of the spectral density as in the main text, but restrict it to a finite support of ΔE centred around $\hbar\delta = 1.5$ meV, corresponding to the detuning of the excitation from the quantum dot transition. For large values of $\Delta E \approx 3$ meV, the memory time of the environment is shortest, while in the limiting case for small widths $\Delta E \to 0$ only a single environment mode energy exists and the memory time becomes infinite.

In all methods, we use a time step width of $\Delta t = 0.1$ ps, compression threshold $\epsilon = 10^{-7}$ and initial bath temperature $T = 0$ K. For ACE, we discretise the continuum ΔE on N_E intervals with a density of states $N_E/\Delta E = 20$ meV^{-1} and we truncate the environment Hilbert space per Boson mode to dimension $M = 2$ or $M = 3$. For this set of parameters, the typical relative difference between exciton populations in the different methods is $\approx 2 \times 10^{-3}$.

In Fig. S.3.1**b**, the computation times needed for the different methods are depicted as a function of the spectral density width ΔE. For large widths $\Delta E \gtrsim 1.4$ meV, we find the Gaussian PT calculation to be faster than both ACE and TEMPO without memory truncation. Note, however, that TEMPO can benefit significantly from memory truncation, as this reduces the length of the MPO chain to be compressed and propagated. Fixing the memory time to $\tau_{\rm mem} = 2.5$ ps in TEMPO leads to the fastest results of all considered methods in the regime of large ΔE. Yet, for smaller widths $\Delta E \lesssim 1.5$ meV, the bath memory time starts to exceed 2.5 ps, which leads to visible deviations in the occupations (not shown). The smaller (disconnected) pink dots in Fig. S.3.1**b** indicate data points where the relative error with respect to Gaussian PT calculations exceeds 1%. For narrow spectral densities, we observe a cross-over rendering ACE faster than all other methods. As shown, the required dimension M per boson mode has a large influence on the run time for ACE.

To summarize, in the special case of Gaussian baths, alternative methods can benefit from the existence of analytical expressions for the influence functional describing the environment, and therefore perform faster than ACE in cases where broad spectral densities lead to short memory times. On the other hand, for narrowly peaked spectral densities that can be well described in terms of a few environment modes, the general method ACE can even outperform specialised methods for Gaussian baths. Finally, it is noteworthy that our computer code produces Gaussian PTs that are completely compatible with the PTs utilised by ACE, paving the way for prospective hybrid approaches for spectral densities with sharp peaks on top of broad continua.

S.4. ENVIRONMENT MODES WITH ANHARMONIC POTENTIALS

In the main text, we present ACE simulations for an open quantum system coupled to a bath of anharmonic environment modes whose free evolution is governed by the Morse potential. Here, we lay out the full numerical treatment starting from the Schrödinger equation of a single environment mode for an arbitrary potential $V(r)$ directly from a numerical representation of the potential on a real space grid.

A. Finite differences to find environment states

We start from the one-dimensional Schrödinger equation for a given potential $V(r)$:

$$H = -\frac{\hbar^2}{2m}\frac{\partial^2}{\partial r^2} + V(r). \tag{S.4.1}$$

We first map this onto a dimensionless ordinary differential equation by introducing a characteristic length scale a_0 and energy scale $\epsilon = \hbar^2/(2ma_0^2)$, and defining the dimensionless coordinate $x = r/a_0$. We then define the dimensionless Hamiltonian

$$h := \frac{1}{\epsilon}H = -\frac{\partial^2}{\partial x^2} + v(x), \tag{S.4.2}$$

$$v(x) := \frac{1}{\epsilon}V(a_0 x), \tag{S.4.3}$$

where $v(x)$ is the dimensionless potential. The dimensionless problem is solved by a finite differences method, where a real space grid $x_j = x_0 + j\Delta x$ with width Δx and N_x sample points is introduced and the second derivative is approximated by

$$\frac{\partial^2}{\partial x^2}f(x_i) = \frac{f(x_{i-1}) - 2f(x_i) + f(x_{i+1})}{\Delta x^2}. \tag{S.4.4}$$

The ODE in Eq. (S.4.2) then takes the form of a symmetric tridiagonal matrix, which is diagonalized numerically.

For simulations in ACE, we work in the truncated energy eigenbasis accounting for only the M lowest energy eigenstates of a given mode. The energy eigenvalues E_i of the original problem are obtained by multiplying the eigenvalues of h with ϵ. The operators describing the system-environment coupling are evaluated in the truncated basis depending on the concrete details of the model. For example, if the system couples to the environment modes via the position operator $\hat{r}$, one has to numerically evaluate matrix elements $\langle i|\hat{r}|j\rangle = a_0\langle i|\hat{x}|j\rangle$ with $i, j \in 0, 1, \ldots, M-1$.

B. Example: Harmonic oscillator

As a reference, we first consider the example of the harmonic oscillator potential $V(r) = \frac{m\omega^2}{2}r^2$. Defining length and energy scales $a_0 = \sqrt{\frac{\hbar}{m\omega}}$ and $\epsilon = \frac{\hbar\omega}{2}$, the corresponding dimensionless Schrödinger equation is

$$h := -\frac{\partial^2}{\partial x^2} + x^2. \tag{S.4.5}$$

Back-transforming the numerically obtained eigenvalues of $h : 1, 3, 5, \ldots$, by multiplying with ϵ, one recovers the series $E_n = \hbar\omega\big(n + \frac{1}{2}\big)$ with $n = 0, 1, 2, \ldots$. From the conventional definition of the harmonic oscillator climbing operators it follows that $a_0\hat{x} = \hat{r} = \sqrt{\frac{\hbar}{2m\omega}}\big(a^\dagger + a\big) = \frac{a_0}{\sqrt{2}}\big(a^\dagger + a\big)$. Consequently, to enable a comparison with the spin Boson model, we consider an environment Hamiltonian for ACE simulations of the form

$$\begin{aligned} H_E &= \sum_k \hbar\omega_k \left(a_k^\dagger a_k + \frac{1}{2}\right) + \sum_k \hbar g_k (a_k^\dagger + a_k)|e\rangle\langle e| \\ &= \sum_k \sum_{j=0}^{M-1} \hbar\omega_k \frac{E_j}{2\epsilon}\sigma_{jj}^k + \sum_k \hbar g_k \sum_{i,j=0}^{M-1} \Big(\sqrt{2}\langle i|\hat{x}|j\rangle\Big)\sigma_{ij}^k\, |e\rangle\langle e|, \end{aligned} \tag{S.4.6}$$

where σ_{ij}^k describes the effect of the single-particle operator $|i\rangle\langle j|$ for the k-th environment mode. As shown in Fig. 5 of the main text, this procedure perfectly reproduces the results of the spin Boson model.

C. Example: Morse potential

The Morse potential [8] is an asymmetric anharmonic potential with a finite number of bound states below a continuum of unconfined states. It is often used to describe molecular vibrations with a finite dissociation energy [9]. It takes the form

$$V(r) = D_e\Big(e^{-2(r-r_e)/a_0} - 2e^{-(r-r_e)/a_0}\Big), \tag{S.4.7}$$

where D_e is the well depth, r_e is the position of the minimum of the potential, and a_0 defines its spatial extent. Here, we use a_0 as the length scale and shift the coordinate system such that $r_e = 0$. The Morse potential is made dimensionless

$$v(x) = \Lambda^2\Big(e^{-2x} - 2e^{-x}\Big) \tag{S.4.8}$$

by introducing the parameter $\Lambda = \sqrt{D_e/\epsilon} = \sqrt{2ma_0^2 D_e/\hbar^2}$. The Morse potential is known to have M bound states [8], where M is the largest integer smaller than $\Lambda + \frac{1}{2}$, with energies

$$E_n = -\epsilon\Big(\Lambda - n - \frac{1}{2}\Big)^2 = \epsilon\Big[-\Lambda^2 + 2\Lambda\Big(n+\frac{1}{2}\Big) - \Big(n+\frac{1}{2}\Big)^2\Big]. \tag{S.4.9}$$

For deep potentials $\Lambda \to \infty$, the spectrum of the lowest states becomes equivalent to that of a harmonic oscillator with $\hbar\omega = 2\epsilon\Lambda$, which is consistent with the second-order Taylor expansion around $r = r_e$ being $V(r) \approx -D_e + \frac{m\omega^2}{2}(r-r_e)^2$. For general Λ, the level spacings between confined states are

$$\Delta E_n = E_{n+1} - E_n = \hbar\omega\Big(1 - \frac{n+1}{\Lambda}\Big). \tag{S.4.10}$$

The energy difference between first excited state and ground state is $\Delta E_g = \hbar\omega\big(1-\Lambda^{-1}\big) = \sqrt{\frac{2\hbar^2 D_e}{ma_0^2}} - \frac{\hbar^2}{ma_0^2}$.

In Fig. 5**a** in the main article, the five bound eigenstates of the Morse potential with $\Lambda = 5$ obtained from numerical finite-differences calculations are depicted. In contrast to harmonic oscillator wave functions, the anharmonicity of the Morse potential manifests itself in the decreasing level spacings for higher states. Furthermore, the wavefunctions are strongly asymmetric leading to nonzero values of the average position operator $\langle i|\hat{x}|i\rangle$ for the i-th state. This non-zero expectation has a significant impact on the system-environment coupling.

Note that the matrix element of the dimensionless position operator $\hat{x}$ between subsequent eigenstates of the Morse potential behaves as $\langle i+1|\hat{x}|i\rangle \to \sqrt{i+1}/\sqrt{2\Lambda}$ for $\Lambda \to \infty$, so that a situation comparable with the independent-boson model in this limit requires an environment Hamiltonian of the form

$$H_E = \sum_k \sum_j \hbar\omega_k \tilde{E}_j \sigma_{jj}^k + \sum_k \hbar g_k \sum_{i,j=0}^{M-1} \Big(\sqrt{2}\langle i|\tilde{x}|j\rangle\Big)\sigma_{ij}^k\, |e\rangle\langle e|, \tag{S.4.11}$$

with $\tilde{E}_j = E_j/\Delta E_g$ and $\langle i|\tilde{x}|j\rangle = \sqrt{\Lambda}\langle i|\hat{x}|j\rangle$.

With nonzero diagonals $\langle i|\hat{x}|i\rangle$ for finite Λ, the asymmetry of the potential leads to the additional effect of a renormalisation of the system excited state energy by a value of $\Delta E = \sum_k \hbar g_k \sqrt{2\Lambda}\,\langle\hat{x}\rangle_E^k = \sum_k \hbar g_k \sqrt{2\Lambda}\,\mathrm{Tr}\big(\hat{x}\rho_E^k\big)$, which depends on the state of the environment.

D. Details of the calculation and parameters

For the ACE simulation depicted in Fig. 5 in the main article, we consider a continuously driven two-level system with system Hamiltonian $H_S = \frac{\hbar}{2}\Omega\big(|e\rangle\langle g| + |g\rangle\langle e|\big)$. The environment is described by the Hamiltonian H_E in Eq. (S.4.11) with parameters ω_k and g_k sampling a Lorentzian spectral density

$$J(\omega) = C\frac{1}{\pi}\frac{\gamma}{(\omega-\omega_c)^2 + \gamma^2}. \tag{S.4.12}$$

We do this by discretising ω_k/Ω equidistantly in the range $[0, 7.5]$ with $N_E = 100$ modes, and setting $g_k = \sqrt{J(\omega_k)\Delta\omega}$, where $\Delta\omega$ is the distance between subsequent ω_k sample points. Here, we set $\hbar = 1$, and fix the parameters of the spectral density to $C = 0.1\Omega^2$, $\gamma = 0.1\Omega$, and $\omega_c = \Omega$. The corresponding values g_k/Ω are plotted in Fig. 5**b** in the main article. The environment modes are initialised with thermal states at temperature $k_B T = 0.5\Omega$.

S.5. SUPERRADIANCE OF TWO QUANTUM EMITTERS

In this section we present an additional illustration of the potential of ACE. We consider the radiative decay of two quantum emitters coherently coupled to the same radiation field as depicted in Fig. S.5.1a. If the distance d between the emitters is much smaller than the wavelength λ associated with the fundamental transitions of the emitters, both emitters couple with the same phase to the radiation field. This gives the Hamiltonian of photon mode k as

$$H_E^k = \hbar\omega_k a_k^\dagger a_k + \hbar g_k \Big[a_k^\dagger \big(|g_1\rangle\langle e_1| + |g_2\rangle\langle e_2| \big) + h.c. \Big], \tag{S.5.1}$$

where $|g_i\rangle$ and $|e_i\rangle$ denote the ground and excited state of emitter $i = 1, 2$ and $a_k^\dagger$ creates a photon in mode k. In analogy to the first example in the main article, our environment is a discretised quasi-continuum of electromagnetic modes with a density of states which would correspond to keeping the Fermi's golden rule rate for the decay of a single emitter, κ, fixed. We admit in general a detuning δ between the transitions of the two emitters, which enters the system Hamiltonian $H_S = \frac{\hbar\delta}{2}\big(|e_1\rangle\langle e_1| - |e_2\rangle\langle e_2|\big)$. The initial conditions are chosen such that both emitters are excited at time $t = 0$.

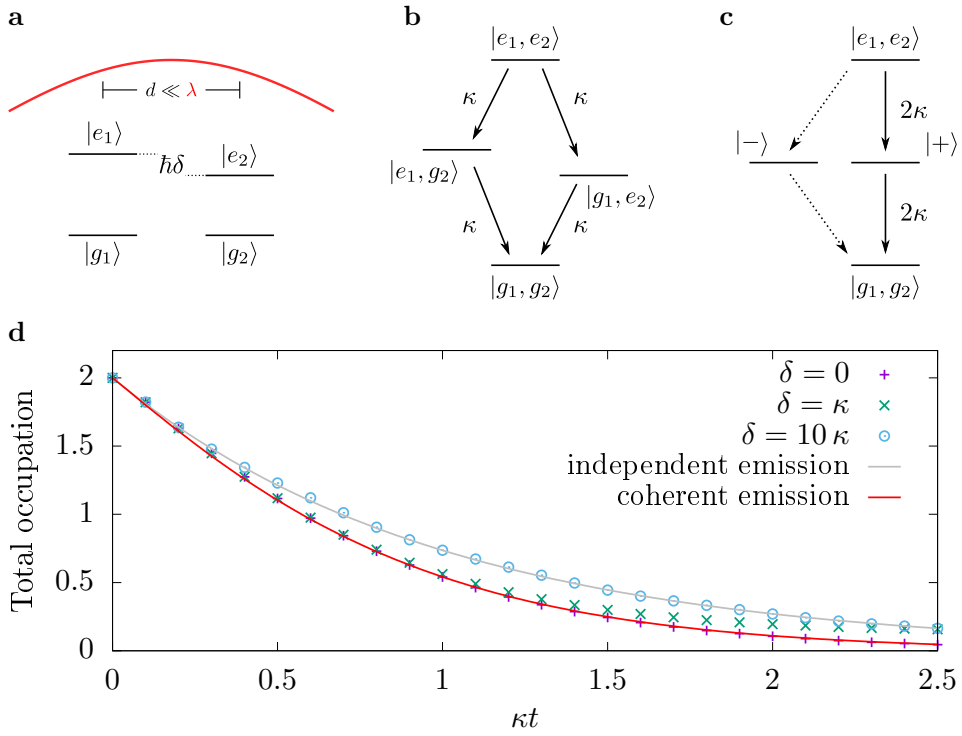

FIG. S.5.1. **Transition between independent and superradiant emission of two proximal optical dipoles. a,** Two quantum emitters detuned by an energy $\hbar\delta$ and separated by a distance d much smaller than the wavelength λ corresponding to the emitter transitions. **b,** Radiative decay of two independent emitters. **c,** Superradiance of two coherently coupled emitters. The transition through the symmetric state $|+\rangle$ has twice the rate compared to that of independent emitters whereas the transition through the antisymmetric state $|-\rangle$ is forbidden. **d,** ACE simulations for different detunings δ and analytic results for independent emission and for coherent emission in the superradiant regime of two emitters.

This situation is interesting as it constitutes a minimal setup for superradiance: If the emitters are distinguishable, e.g., if the detuning δ is large, both emitters radiatively decay with a rate κ, as depicted in Fig. S.5.1b, so that the sum of the occupations decays as $2\exp(-\kappa t)$. If, however, the emitters are indistinguishable $\delta = 0$, the coherent coupling makes it necessary to derive the respective decay rates in the symmetrised basis including the states $|\pm\rangle = \big(|e_1, g_2\rangle \pm |g_1, e_2\rangle\big)/\sqrt{2}$. The dipole for transitions involving the symmetrised state $|+\rangle$ is larger than that of a single emitter, whereas it is zero of the antisymmetrised state $|-\rangle$. Consequently, $|-\rangle$ is dark and the decay takes place from $|e_1, e_2\rangle$ to $|+\rangle$ and from $|+\rangle$ to $|g_1, g_2\rangle$ with the rate 2κ, as depicted in Fig. S.5.1c. Taking into account the dynamics of the intermediate state occupations, the total occupation of the two indistinguishable emitters is $n_{\mathrm{tot}} = 2(1 + \kappa t)\exp(-2\kappa t)$ [10].

Figure S.5.1d shows the total occupation of the two emitters for $\delta = 0$, $\delta = \kappa$, and $\delta = 10\kappa$ obtained using the ACE method as well as the analytic results corresponding to the case of distinguishable and indistinguishable emitters.

For $\delta = 10\kappa$, the ACE simulation agrees with the exact result for independent emitters, while for $\delta = 0$ the result for coherently coupled indistinguishable emitters is reproduced. In the intermediate regime $\delta = \kappa$, the dynamics can be understood qualitatively by interpreting δ as a perturbation facilitating a rotation from the symmetric $|+\rangle$ to the antisymmetric $|-\rangle$ state. As the latter is dark, the total occupation at long times is found to be even slower than the decay of independent emitters.

This example demonstrates that in a situation where rate equations crucially depend on the basis in which they are derived, the ACE reproduces correct results independent of the basis. Thus, even in Markovian scenarios, ACE simulations can have an advantage over conventional techniques in that it can be applied straightforwardly in an arbitrary basis.

On the technical side, we have solved the dynamics of a four-level system, showing that the method is not restricted two-level systems. To achieve this, we have made use of the fact that the matrices $\mathcal{Q}^{(\alpha_l,\tilde{\alpha}_l)}_{d_l d_{l-1}}$ are identical for some combinations of $(\alpha_l, \tilde{\alpha}_l)$. This can be done by analogy with the method devised for iQUAPI [11], using a decomposition into groups with identical couplings. With this, we only compute non-redundant values, which reduces the 256 possible combinations of $(\alpha_l, \tilde{\alpha}_l)$ to 18. These groups can be identified numerically from the specified environment Hamiltonians H_E^k, so that this step is also automated.

S.6. DISPERSIVE COUPLING

Here, we consider a toy model of a TLS dispersively coupled to a multi-mode microcavity, in order to demonstrate several remaining aspects of the generality of ACE that were not covered in previous examples. Specifically: non-Gaussian interactions due to non-linear system-environment coupling, time-dependent driving of the environment, and non-unitary evolution of the environment modes.

A common situation in which non-Gaussian environments emerge is when the coupling to the environment is non-linear in environment mode creation and annihilation operators. The simplest case is that of quadratic system-environment coupling, as in the case of dispersive coupling described by an interaction Hamiltonian $H_I = \sum_k \hbar g_k a_k^\dagger a_k \sigma_z$. Such a coupling arises, e.g., in an effective description of a two-level system (TLS) coupled to a microcavity in the limit where the detuning between TLS and cavity is much larger than the coupling strength [12]. The main effect of dispersive coupling is that the TLS transition energy experiences a shift depending on the cavity photon number and, vice versa, the cavity mode energy is modified by the excited state population n_e of the TLS. The former paves the way for quantum non-demolition measurement of the cavity photons by probing the TLS [12].

We consider the setting depicted in Fig. S.6.1**a**: A TLS is coupled to a microcavity that supports multiple discrete photon modes which can be individually addressed by external driving. The cavity modes are assumed to be detuned far enough from the fundamental TLS transition that the TLS-cavity coupling is well described by a dispersive interaction. The initially empty cavity modes are then driven one-by-one by short external pulses centred around times τ_k, $k = 1, 2, 3, 4$. As a result of the dispersive coupling, this leads to a shift of the TLS transition energy, which is probed by driving the TLS directly and continuously with a driving field (driving strength Ω) that is resonant with the bare TLS transition frequency.

To this end, we apply ACE to the Hamiltonian $H = H_S + \sum_k H_E^k$ with

$$H_S = \frac{\hbar}{2}\Omega\big(|e\rangle\langle g| + |g\rangle\langle e|\big), \tag{S.6.1}$$

$$H_E^k = \hbar g a_k^\dagger a_k \sigma_z + \hbar\omega_k a_k^\dagger a_k + \frac{\hbar}{2}G_k(t)\big(a_k^\dagger e^{-i\omega_k t} + a_k e^{i\omega_k t}\big), \tag{S.6.2}$$

using model parameters $\Omega/g = 8.5\pi/10$, and $\omega_k/g = 10 + k$, as well as convergence parameters $g\Delta t = 0.01$ and $\epsilon = 10^{-9}$ accounting for up to four bosons per cavity mode.

In a first step, to aid understanding of the general case, instead of modelling the cavity mode excitation explicitly by pulses with envelope $G_k(t)$, we consider the instantaneous preparation of one-photon Fock states. This corresponds to applying creation operators $a_k^\dagger$ to the forward propagating part of the environment mode Liouville propagator, and the annihilation operators a_k to the backward propagating part at time $g\tau_k = 10k$ for the k-th mode. The results are depicted in Fig. S.6.1**b** and indeed show that whenever a photon is added to a cavity mode, the observed Rabi oscillations of the TLS become more and more off-resonant as indicated by their decreasing amplitude and increasing frequency.

Next, we consider explicit time-dependent driving of the cavity modes by Gaussian pulses with

$$G_k(t) = \frac{A_k}{\sqrt{2\pi}\sigma}\exp\left[-\frac{(t-\tau_k)^2}{2\sigma^2}\right], \tag{S.6.3}$$

with $\sigma = \tau_{\mathrm{FWHM}}/(2\sqrt{2\ln 2})$, $g\tau_{\mathrm{FWHM}} = 0.2$, and $A_k = 2$. These parameters are chosen such that after the k-th pulse the cavity photon number $\langle a_k^\dagger a_k\rangle \approx 1$. As can be seen in Fig. S.6.1**c**, the TLS dynamics is now more complicated. As seen for instantaneous Fock state preparation, the oscillation amplitudes are reduced when another cavity mode is excited, however the signal now involves more than a single frequency. This is due to the fact that the external driving as described by H_E^k induces coherent states as opposed to one-photon Fock states, so that now contributions corresponding to Fock states with $n = 0$, $n = 2$, $n = 3$, and $n = 4$ are also excited with a finite probability. The joint state of TLS and cavity is therefore best discussed in terms of sectors with fixed photon and excitation numbers n and n_e, respectively. This can be illustrated by considering a single cavity mode, where the total system plus environment is tractable without compression, so that the total system can be propagated as a single, closed quantum system. This provides access to the full state including photon-number-resolved TLS populations $|e, n\rangle$, where $|e\rangle$ refers to the excited state of the TLS and n is the cavity photon number. These are shown in Fig. S.6.1**d**. This calculation agrees with the ACE simulations in Fig. S.6.1**c** up to time τ_2, when a second mode becomes involved. This demonstrates that the complicated evolution of the TLS occupation is just a sum of contributions from individual n-photon sectors, each evolving with a single, well-defined frequency.

Finally, because the starting point of ACE are the propagators of the environment modes in Liouville space, it is straightforward to include non-unitary evolution of the environment, such as loss terms that directly affect the

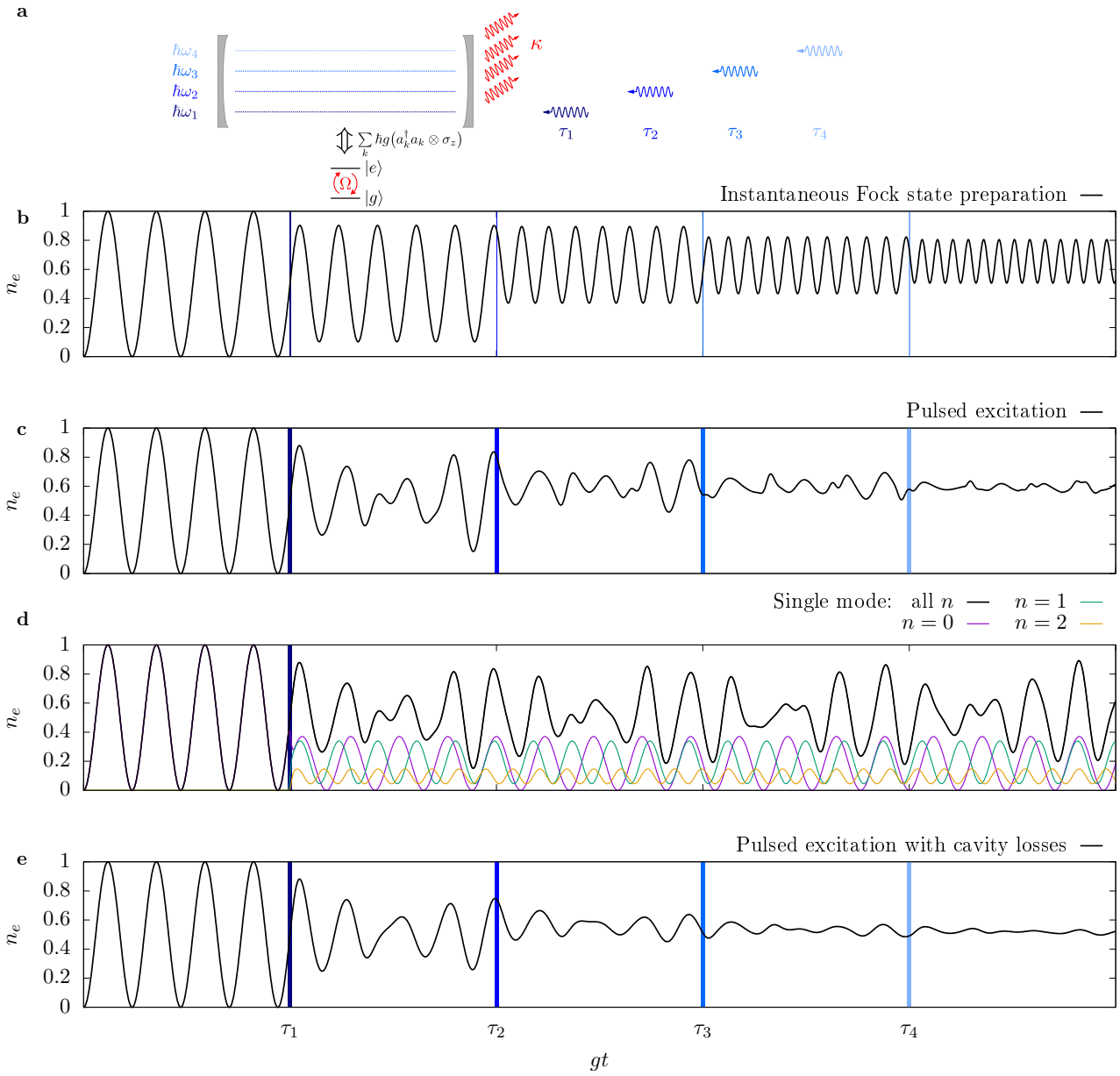

FIG. S.6.1. **a**: Sketch of a TLS dispersively coupled to a multi-mode microcavity, resulting in changes of the effective transition frequency of the TLS when the cavity modes are driven externally by pulses arriving at times τ_k. The TLS itself is continuously driven with bare Rabi frequency Ω, allowing one to detect signatures brought about by changes of the transition frequency. Photons are lost from the cavity modes with rate κ (but $\kappa = 0$ for panels **b**-**d**) **b**: Evolution of the excited state population n_e when the pulses exciting the cavity modes are replaced by an instantaneous change of the state of the i-th cavity mode from the vacuum to the one-photon Fock state at time τ_i indicated by blue vertical lines. **c**: Excited state population when the cavity modes are excited by Gaussian pulses. **d**: Numerical simulation accounting for a single cavity mode as part of the system. The total TLS excitation is presented as well as the photon-number-resolved TLS excitations. **e**: Like **c** but additionally accounting for non-zero photon loss rate $\kappa = 0.1g$.

dynamics of the environment modes. Including Lindblad terms

$$\kappa\left[a_k\rho a_k^\dagger - \frac{1}{2}\left(a_k^\dagger a_k\rho + \rho a_k^\dagger a_k\right)\right] \tag{S.6.4}$$

describing the loss of photons with rate $\kappa = 0.1g$ to the environment propagator, one obtains the results depicted in Fig. S.6.1**e**. While generally very similar to the behaviour in the case without losses shown in Fig. S.6.1**c**, losses with

a finite rate κ are found to lead to more efficient dephasing as they intermix sectors with different photon numbers.

[1] A. M. Childs, Y. Su, M. C. Tran, N. Wiebe, and S. Zhu, Theory of trotter error with commutator scaling, Phys. Rev. X **11**, 011020 (2021).

[2] C. Eckart and G. Young, The approximation of one matrix by another of lower rank, Psychometrika **1**, 211 (1936).

[3] E. Ye and G. K.-L. Chan, Constructing tensor network influence functionals for general quantum dynamics, The Journal of Chemical Physics **155**, 044104 (2021).

[4] M. Cygorek, Automated Compression of Environments (ACE), http://dx.doi.org/10.5281/zenodo.5214128 (2021).

[5] M. R. Jørgensen and F. A. Pollock, Exploiting the causal tensor network structure of quantum processes to efficiently simulate non-markovian path integrals, Phys. Rev. Lett. **123**, 240602 (2019).

[6] A. Strathearn, P. Kirton, D. Kilda, J. Keeling, and B. W. Lovett, Efficient non-markovian quantum dynamics using time-evolving matrix product operators, Nat. Commun. **9**, 3322 (2018).

[7] N. Makri and D. E. Makarov, Tensor propagator for iterative quantum time evolution of reduced density matrices. I. Theory, J. Chem. Phys. **102**, 4600 (1995).

[8] P. M. Morse, Diatomic molecules according to the wave mechanics. ii. vibrational levels, Phys. Rev. **34**, 57 (1929).

[9] M. Bramberger and I. De Vega, Dephasing dynamics of an impurity coupled to an anharmonic environment, Phys. Rev. A **101**, 012101 (2020).

[10] M. Gross and S. Haroche, Superradiance: An essay on the theory of collective spontaneous emission, Physics Reports **93**, 301 (1982).

[11] M. Cygorek, A. M. Barth, F. Ungar, A. Vagov, and V. M. Axt, Nonlinear cavity feeding and unconventional photon statistics in solid-state cavity qed revealed by many-level real-time path-integral calculations, Phys. Rev. B **96**, 201201 (2017).

[12] A. Blais, R.-S. Huang, A. Wallraff, S. M. Girvin, and R. J. Schoelkopf, Cavity quantum electrodynamics for superconducting electrical circuits: An architecture for quantum computation, Phys. Rev. A **69**, 062320 (2004).